SEISMOLOGY

High seismic attenuation at a mid-ocean ridge reveals the distribution of deep melt

Zachary C. Eilon[1,2,3]* and Geoffrey A. Abers[1,4]

At most mid-ocean ridges, a wide region of decompression melting must be reconciled with a narrow neovolcanic zone and the establishment of full oceanic crustal thickness close to the rift axis. Two competing paradigms have been proposed to explain melt focusing: narrow mantle upwelling due to dynamic effects related to in situ melt or wide mantle upwelling with lateral melt transport in inclined channels. Measurements of seismic attenuation provide a tool for identifying and characterizing the presence of melt and thermal heterogeneity in the upper mantle. We use a unique data set of teleseismic body waves recorded on the Cascadia Initiative's Amphibious Array to simultaneously measure seismic attenuation and velocity across an entire oceanic microplate. We observe maximal differential attenuation and the largest delays ($\Delta t_S^* \sim 1.7$ s and $\delta T_S \sim 2$ s) in a narrow zone <50 km from the Juan de Fuca and Gorda ridge axes, with values that are not consistent with laboratory estimates of temperature or water effects. The implied seismic quality factor ($Q_s \leq 25$) is among the lowest observed worldwide. Models harnessing experimentally derived anelastic scaling relationships require a 150-km-deep subridge region containing up to 2% in situ melt. The low viscosity and low density associated with this deep, narrow melt column provide the conditions for dynamic mantle upwelling, explaining a suite of geophysical observations at ridges, including electrical conductivity and shear velocity anomalies.

INTRODUCTION

Mid-ocean ridges (MORs) comprise the largest volcanic systems worldwide. Observations of focused MOR volcanism (*1*) and the establishment of full oceanic crustal thickness within 1 to 3 km of the axis (*2*) stand in contrast with models that include decompression melting over an approximately 100- to 200-km-wide triangular melt region (*3*). Buoyancy effects (*4*) and lateral transport (*5*–*7*) have separately been invoked to explain a narrow zone of melt production, with the latter being preferred in the absence of definitive evidence for abundant in situ melt beneath the ridge axis (*8*). Hints of deep melt come from observations of low seismic velocities and elevated electrical conductivity to depths of 200 km (*9*–*11*), well below the depth predicted from ridge temperature structure. However, the quantity, distribution, and ascent pathways of melt at MORs are poorly understood. Simultaneous observations of velocity and seismic attenuation can help discriminate the importance and fraction of melt (*12*). Mantle attenuation at MORs has received relatively little attention; global models show low Q_S (50 to 60) in the upper 200 km close to the ridge (*12*), whereas a single regional study found surprisingly high Q_S (≈70) at the East Pacific Rise (EPR) using surface waves, at odds with low shear velocities (*13*). Surface wave studies provide good vertical resolution but suffer from lateral smearing that may obscure short-wavelength anomalies. Measurements of body wave travel times and attenuation hold promise for achieving sufficiently dense spatial sampling to place bounds on the temperature and melt character of an MOR.

[1]Lamont-Doherty Earth Observatory, Columbia University, 61 Rte. 9W, Palisades, NY 10964, USA. [2]Department of Earth, Environmental, and Planetary Sciences, Brown University, 324 Brook Street, Providence, RI 02912, USA. [3]Department of Earth Sciences, University of California, Santa Barbara, 1006 Webb Hall, Santa Barbara, CA 93106, USA. [4]Department of Earth and Atmospheric Sciences, Cornell University, 2122 Snee Hall, Ithaca, NY 14853, USA.
*Corresponding author. Email: eilon@geol.ucsb.edu

DATA AND METHODS

The Amphibious Array deployment of the Cascadia Initiative provides an unprecedented opportunity to study an entire ocean plate from ridge to trench (*14*). We use broadband ocean bottom seismometer (OBS) data from the first 3 years of the Cascadia deployment (September 2011 to September 2014), with 87 unique stations in an approximately 70-km-spaced grid across the Gorda and Juan de Fuca (JdF) plates. We measure differential attenuation (Δt*) of teleseismic *P* and *S* waves (Δt_P^* and Δt_S^*, respectively) recorded on this array by measuring pairwise relative phase and amplitude spectra using a comb of filters and then solving a constrained least-squares problem to retrieve relative attenuation at all stations across the array (Fig. 1). At the same time, we measure *P*- and *S*-wave differential travel times using cross-correlation. Incidence angles are 18° to 36° for the teleseisms we recorded. Our method is only sensitive to differential attenuation and time delays; we report values of Δt^* relative to a reference value of zero taken as the average values for stations on 4– to 8–million year (My) crust. Tests for frequency dependency of *Q* of the form $Q(\omega) = Q_0\,(\omega/\omega_0)^{\alpha}$ demonstrate that best-fitting α is approximately 0.2. We present attenuation results corrected to 1 Hz assuming that $\alpha = 0.27$, in line with previous observations (*15*) and close to experimentally estimated α values (*16*, *17*).

RESULTS

Patterns of back-azimuthal and interstation variations indicate spatial coherency to observed Δt^* (Figs. 1 and 2). Δt_S^* up to 1.7 s is recorded across a range of back azimuths at all stations within 50 km of the ridge axes. These observations represent some of the largest values of differential attenuation observed worldwide, indicating extremely strong gradients in Q_S. The Gorda and southern JdF ridges have the highest values of Δt_S^*, whereas stations on the northern part of the JdF ridge record ~1.0 s lower Δt_S^* (Fig. 3). Between 2 and 4 My (50 to 100 km from the ridge), there is a 1-s decrease in Δt_S^* toward older seafloor; stations on older crust are less attenuating, with no statistically significant age correlation in Δt_S^* between 4 and 8 My. The reduction in attenuation is sharp for the JdF, but more diffuse for the Gorda ridge, consonant with

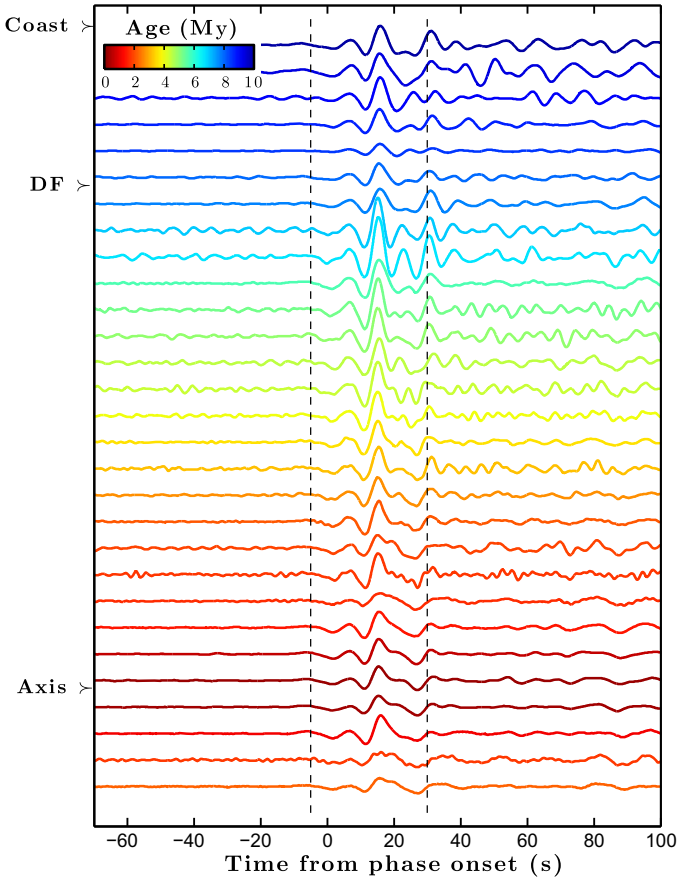

Fig. 1. Example of *S* waves recorded at JdF OBS stations from an event on 3 April 2014 at a distance of ~84°, from a back azimuth of ~129°. T-component displacement seismograms are aligned by cross-correlation, colored by age, arranged by distance to ridge, and plotted with a 0.05- to 2-Hz fourth-order Butterworth filter. Dashed lines, data window for calculation of spectra. DF, deformation front.

a broad region of low velocities beneath Gorda in this study and in other studies (*18*). Our data do not constrain the western limit of the high-attenuation zone. JdF ridge stations evince a slight (27%) bias toward higher Δt_S^* for arrivals from the west, suggestive of ridge asymmetry observed for seismic velocities (*18*). Projected ray paths (see the Supplementary Materials) indicate that most of the attenuation signal originates west of the ridge for the southern JdF but, without more stations on the Pacific plate, we cannot discern whether the attenuating region is strongly asymmetric or confined to shallow depths. Δt_P^* values are systematically smaller and contain more scatter but overall show highly similar results to *S* waves, with highest attenuation ($\Delta t_P^* \leq 0.5$ s) at the ridge axis and a steady decrease from 2 to 7 My.

Differential travel times ($\delta T_{S,P}$) qualitatively agree with the attenuation results (Figs. 2 and 3): The slowest arrivals ($\delta T_S \leq 2.5$ s delay) are recorded close to the ridge axes, with relatively small travel time residuals (indicating faster structure) at greater plate ages. Consistent with attenuation, the southern JdF ridge stations are slower (by ~0.5 s for *S* waves) than their counterparts north of ~47°N. Unlike for attenuation, travel time residuals throughout the Gorda deformation zone are large and barely decrease with age (Fig. 3). For both JdF and Gorda plates, the $\delta T_{S,P}$ values do not mimic the sharp step at 2 My seen in the attenuation results. As expected, the *S* waves display greater travel time variations than *P* waves, consonant with anelastic effects more strongly affecting the shear modulus.

On the continental shelf, we observe high apparent attenuation ($\Delta t_S^* >$ 2.5 s) and travel time delays ($\delta T_S > 3.0$ s). These signals are likely the product of shallow scattering or soft-sediment absorption processes; Δt_S^* varies by >2.0 s between stations separated by just 15 km, requiring a near-surface source for the variability and ruling out the possibility of an origin in the mantle. Land stations on the continent show higher mean values of apparent attenuation than oceanic stations, likely resulting from dissipation and scattering within the continental crust and volcanic arc system. This finding (and the range of onshore $\Delta t_{P,S}^*$) is consistent with previous studies that have shown high attenuation in the Pacific Northwest compared to the rest of the continental United States (*19*), but further interpretation is beyond the scope of this study.

Linear fitting of Δt_S^* versus Δt_P^* yields an estimated $Q_P/Q_S = 2.44^{+0.43}_{-0.72}$ (95% confidence intervals), assuming negligible Δt^* at the least-attenuated station. This is close to the theoretical value of $Q_P = 2.25\ Q_S$ for a Poisson solid (*20*) [or 2.46 for the Preliminary Reference Earth Model (*21*)], indicating that the assumption of negligible bulk modulus attenuation is extremely good in the oceans. The slope of station-averaged δT_S versus δT_P constrains best-fitting $\delta \ln V_S / \delta \ln V_P$ below the array to be $1.63^{+0.72}_{-0.28}$ (95% confidence intervals). This falls in the range predicted for temperature-controlled wave speeds (*22*) but within uncertainty of the theoretical value of 2.25 for a Poisson solid with perturbations to only the shear modulus, as expected if melt and not temperature drives the *Q* variations (*22*). Thus, we cannot rule out the possibility that velocity heterogeneities are driven by melt, rather than temperature.

DISCUSSION

The central result of this study is the surprisingly large $\Delta t_S^* \approx 1.7$ s measured at the ridge, relative to the off-axis reference value. In accordance with predicted perturbations to temperature and the onset of melt (*23*), global and local mantle velocity models indicate that the seismic signature of passive spreading ridges extends down to depths of ~200 km (*9*), and Δt* measured between *S* and *sS* waves seems to be accrued in the mantle no deeper than 200 km (*24*). The sharp transition in attenuation between on- and off-axis stations east of the JdF ridge indicates that much of the attenuation takes place shallower than the depth at which ray paths to off-ridge stations pass beneath the ridge (~150 km). We surmise that contributions to ridge-related attenuation also originate above this depth, requiring a mean value for $Q_S \approx 25$ beneath the ridge, as an upper bound [assuming $Q_S \approx 90$ in the 4- to 8-My reference region (*12*)]. $Q_S < 90$ in the off-ridge reference region would lower the on-ridge Q_S estimate. $Q_S \approx 25$ is substantially less than the average $Q_S \approx 70$ observed at the MELT (Mantle Electromagnetic and Tomography experiment) region (*13*), although it agrees with ridge attenuation models that fit EPR shear velocities (*25*). The discrepancy may partly arise from differences in lateral resolution between our body wave data and laterally averaged surface wave attenuation, but the faster-spreading EPR may also be less attenuating overall than the JdF. The lowest previously observed values of mantle $Q_S < 25$ were imaged at the Lau back-arc (*26*).

Evaluating extrinsic effects

Our approach measures only apparent attenuation. Long-period focusing, short-period defocusing, or frequency-dependent scattering could cause us to overestimate intrinsic anelastic dissipation (*27*, *28*). We show that measured Δt* cannot arise from a comparative excess of (focused) long-period energy at ridge stations (see the Supplementary Materials). These stations have lower absolute amplitudes than abyssal plain stations at all frequencies but are increasingly diminished at higher

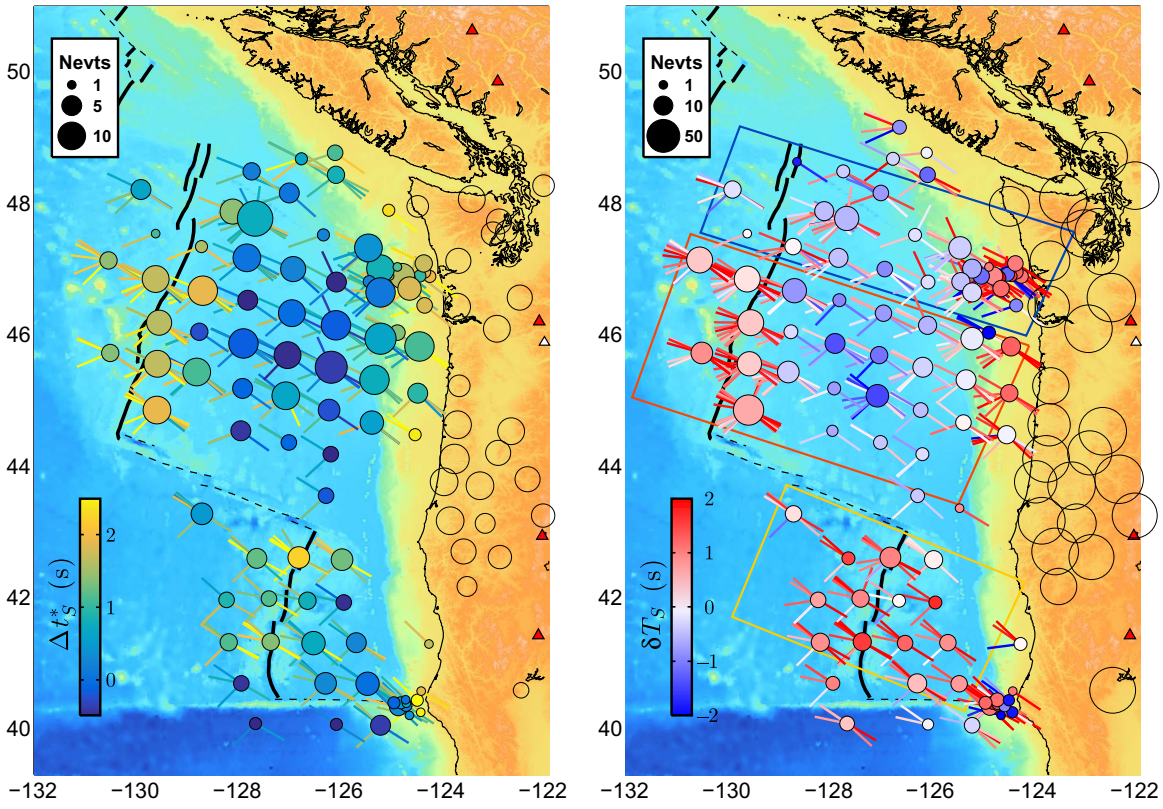

Fig. 2. *S*-wave Δt^* (left) and δT (right) recorded at OBS stations. Radial spokes show individual arrivals at their incoming azimuth, whereas central circles show least-squares station average terms. Open circles show land stations used to link JdF and Gorda arrays. Boxes show three areas: north JdF (blue), south JdF (red), and Gorda (yellow).

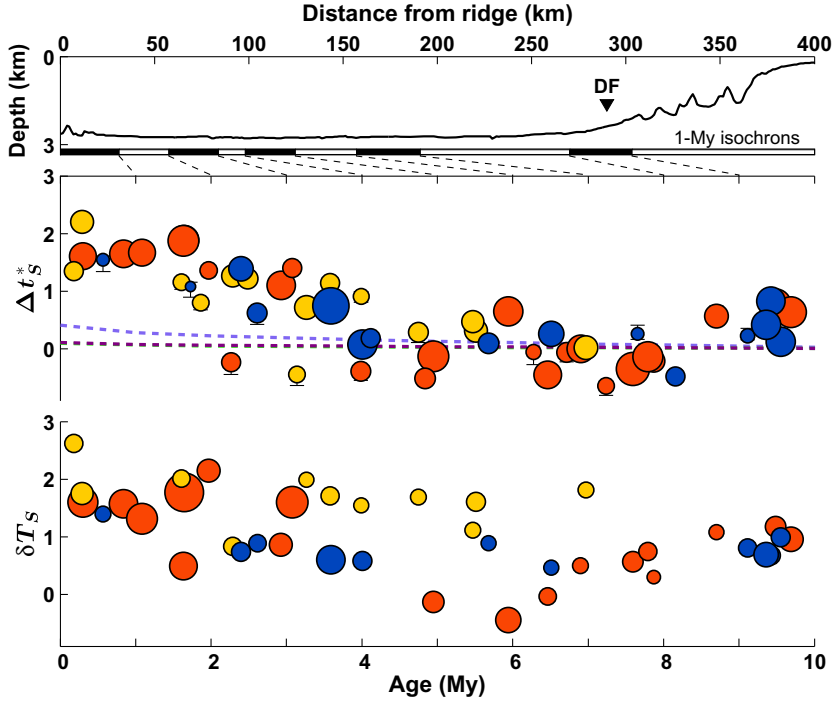

Fig. 3. Station-averaged *S*-wave Δt^* and δT as a function of crustal age, relative to the mean value for 4- to 8-My seafloor. A representative west-northwest–east-southeast bathymetric profile at 46.8°N (top) includes deformation front and isochrons reflecting an irregular age-distance relationship. Colors relate to geographic area (Fig. 2) and point size scales with the number of individual observations contributing to the average. Superimposed lines show predictions of differential attenuation due to the effect of temperature alone, assuming half-space cooling and using laboratory-derived anelastic scaling relationships (see the Supplementary Materials). 2σ uncertainties for Δt^* are shown where they exceed the symbol size. δT uncertainties are ~0.3 s.

frequencies, as expected from intrinsic attenuation. Previous studies show that strongly defocused short-period energy would be highly delayed (by up to ~5 s) relative to unscattered arrivals (*29*). This is not consistent with moderate (<2.5 s) travel time residuals at the ridge or the good simultaneous fitting of both amplitude and phase spectra. Finally, the estimated Q_P/Q_S = 2.44 indicates negligible bulk modulus attenuation, whereas most models of elastic scattering typically predict $Q_P \approx Q_S$ (*27*). Elastic scattering would produce strong coda energy for arrivals with the highest apparent attenuation, whereas we observe the opposite: More high-frequency energy persists after the main arrival for the least-attenuated stations (Fig. 1). The exceptions that prove the rule are measurements from the shallow stations on the accretionary prism, which record low Q_P/Q_S, high Δt_P^* and Δt_S^* that vary by up to 3.0 s over short distances, and energetic high-frequency coda. These signals evince the hallmarks of scattering or soft-sediment effects that are conspicuously absent for stations at the ridge axis. We cannot rule out the possibility that elastic scattering contributes partially to apparent attenuation, but the data are inconsistent with it playing a major role.

Respective roles of temperature, water, and melt

In oceanic lithosphere, temperatures are well constrained by our robust understanding of conductive plate cooling, corroborated by bathymetry, heat flow, and geochemical observations. Using several groups' experimentally constrained anelastic scaling relationships (*16*, *30*, *31*), we compute the predicted Q_S and velocity beneath an MOR that arise from temperature heterogeneity alone (Fig. 3). By comparing a station on the ridge axis with a station 300 km away (Table 1), we find that attenuation resulting only from temperature variation predicts $\Delta t_S^* \leq$ 0.21 s. This is an order of magnitude less than the observed values, and the corresponding predicted δT_S is three times less than the observed values. Thermal effects alone cannot explain the observed attenuation.

We take an ad hoc approach to simulate the observed attenuation signal, seeking to quantitatively test the potential role of attenuation due to grain size, water, and melt by systematically adding distinct contributions from a number of notional upper mantle structures (Fig. 4; see Materials and Methods for details). Isolation of any one factor is made more complex by the linkages between these parameters: Water promotes melting, melt dehydrates the solid matrix, and viscosity controls grain sizes through strain rate. Understanding feedbacks between these factors remains a modeling and experimental challenge.

Turner *et al.* (*32*) present MOR models involving dynamically evolving equilibrium grain size that include a modest (~10 ×) strain rate increase in a narrow region beneath the ridge axis and in side lobes immediately beneath the cooling plates. The concomitant grain size reduction will boost attenuation at the ridge axis, but we calculate that this effect will not be greater than Δt_S^* ~ 0.2 s. However, low grain sizes could also lead to axial melt focusing and larger in situ melt retention through surface energy–driven pressure gradients (*33*). The dynamic evolution of grain size is a major uncertainty in our analysis. Experiments characterizing grain growth in a multiphase assemblage that includes partial melt do not exist, to our knowledge. If the presence of melt in the upwelling region limits grain growth rates (*34*), then the relatively diminished grain sizes would also boost attenuation beneath the ridge axis.

Water bound in nominally anhydrous mantle minerals influences MOR dynamics through weakening effects that may also enhance seismic dissipation (*35*). However, although bound H_2O enhances diffusional processes that promote anelasticity, it also augments grain growth rates, yielding a modest net effect on attenuation (*26*). This is reflected (Table 1) in <0.1 s of increased Δt_S^* calculated for a narrow, water-fluxed region due to upwelling beneath the dry solidus at the ridge axis (*36*).

Low seismic wave speed (*9*, *11*) and high electrical conductivities (*10*) are strong evidence that melt plays an important role in controlling the physical properties of MOR mantle down to depths of >200 km. We find that a model with melt in a rectangular region down to a depth of 120 km requires 2% melt throughout to produce the required 1.7 s of Δt_S^*. This box has an average $Q_S \approx 18$ at 1 Hz. This simple model likely overstates the melt fraction at depth beneath the ridge; hydrous melting is not thought to yield this much in situ melt (*37*), and the poroelastic effect of melt means that this model predicts differential travel times that exceed observations by ~50%. A more "realistic" model comprises distinct regions of dry isentropic melting [0 to 60 km (*38*)], wet melting [60 to 120 km (*37*)], and deep carbonated melting [120 to 180 km (*23*)] that contribute Δt_S^* of ~0.6, ~0.5, and ~0.6 s, respectively, reducing Q_S in each region to ~20. The resultant $\Delta t_S^* \approx 1.9$ s (Table 1) slightly overpredicts attenuation, perhaps indicating that some carbonated melting also occurs off-axis, reducing the differential value of t^*. Predicted *P* attenuation and *S* and *P* travel times also fit observed values, within error. Note that we use an older parameterization of laboratory attenuation measurements (*30*), which provides the best fits to the data given our assumptions of small melt fraction. A newer parameterization of the experiments (*16*) can also reproduce the observed signal if we allow for more in situ melt, or an enhanced melt chemical effect, but predicts a viscosity drop that is greater by an order of magnitude (table S1).

If the low-*Q* structure extended as deep as 250 km, then the mean Q_S beneath the ridge would be 34, rather than 20 to 25. However, we would expect a 250-km-deep upwelling region to be visible to off-axis stations, whereas (at least for JdF) the lateral gradient in Δt_S^* is sharp (Fig. 2). A west-dipping or asymmetric attenuating structure may enhance the sharpness of the Δt_S^* transition for stations east of the ridge. Our model, although nonunique, meets the constraints of a strong, ≤150-km-deep attenuation confined to the ridge axis with minimum complexity.

Our analysis indicates that reasonable quantities of deep subaxial melt [$\phi \leq 2\%$ everywhere, consistent with estimates from U-series disequilibria (*39*)] can reproduce observed differential attenuation at ridge stations, even discounting a large effect from carbonated melt.

Table 1. Predicted maximum differential attenuation and travel time for custom MOR models using the method of Faul and Jackson (*30*). Columns are as follows: (1) model conditions; (2) viscosity reduction between 0- and 10-My mantle, averaged between depths of 50 and 100 km; (3) maximum differential t_S^* between the ridge axis and the farthest flank; (4) same as (3), but for *P* waves; (5) maximum differential *S* wave travel time between the ridge axis and the farthest flank; (6) same as (5), but for *P* waves.

Model	$\frac{\tau_{M_{10\ My}}}{\tau_{M_{Ridge}}}$	Δt_S^*	Δt_P^*	δT_S	δT_P
Observations		~1.7	~0.4	~2.0	~0.7
Temperature only	1.1	0.21	0.05	0.69	0.36
ϕ = 2% box (120 km)	261.2	1.67	0.42	3.11	1.10
① Temp. + $\dot{\epsilon}$	3.6	0.34	0.09	0.80	0.39
② + H_2O	4.6	0.42	0.11	0.88	0.41
③ + dry melt	41.9	1.02	0.26	1.76	0.66
④ + hydrous melt	135.2	1.46	0.37	2.26	0.78
⑤ + carbonated melt	186.4	1.90	0.48	2.71	0.89

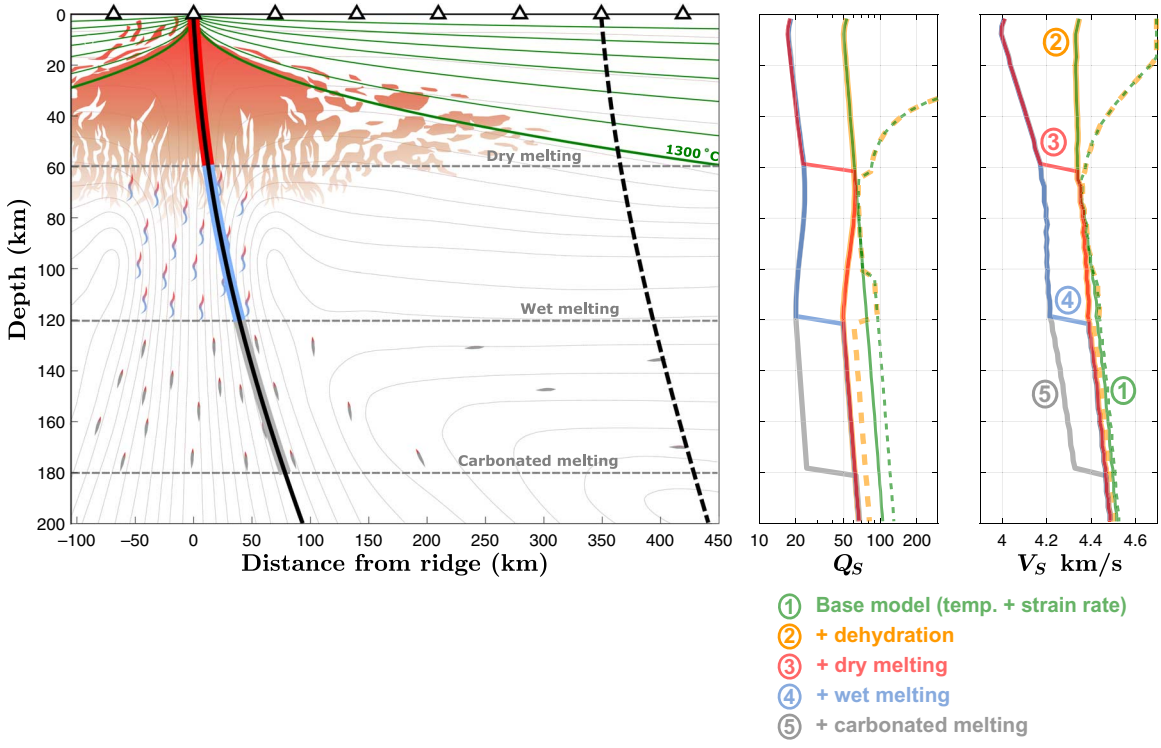

Fig. 4. Schematic of MOR showing several contributions to seismic structure, including temperature (green lines are 200°C isotherms except where stated), strain rate [solid flow streamlines in brown, modified after the work of Braun *et al.* (*41*)], and melt regimes. Profiles of Q_S and V_S along rays incident at stations on 0-My (solid line) and 10-My (dashed line) crust are shown on the right. Melt fraction in the carbonated melt region is 0.01%, melt fraction in the hydrous melt region is 0.01 to 0.2%, and melt fraction in the dry melt region is 0.2 to 2%. See Materials and Methods for details.

Incorporating mineral physics arguments that scale diffusion creep rates to attenuation (*17*, *26*), the values of Q_S in our model correspond to at least a ~150 × viscosity reduction between depths of 50 and 150 km (Table 1). Although this quantitative estimate is linked to several assumptions in our model, a qualitative weakening effect of partial melt at the grain boundaries is well established for crystalline aggregates (*40*).

Dynamic upwelling

Together with melt buoyancy, subaxial viscosity reduction would tend to promote dynamic mantle upwelling that results in a strain localization feedback, concentrating upwelling in a narrow zone beneath the axis (*3*, *41*). Grain sizes may evolve to enhance this effect (*32*). The viscosity increase associated with dehydration likely produces a zone of most strongly focused upwelling at depths of 120 to 60 km (*41*). At shallower depths, although melt reduces viscosity at the ridge axis, the high viscosity of dry oceanic lithosphere will diminish dynamic focusing. Concentrated upwelling may extend deeper than 120 km; in zones of upwelling, low-viscosity carbonatitic melts that wet grain boundaries (*42*) could substantially reduce mantle viscosity, creating a positive feedback between upwelling, melting, and viscosity reduction. Magnetotelluric studies support the presence of >60-km-deep melt (both hydrous and carbonated) at ridge axes (*10*, *43*).

Dynamic buoyancy effects at MORs explain a suite of observations not easily reconciled with passive mantle upwelling. For instance, conservation of mass requires that concentrated axial upwelling result in off-axis downwelling of cooler material, causing faster cooling of the young oceanic plate. This explains why seismic velocities within the JdF and Pacific plates increase with plate age faster than predicted from conductive cooling alone (*18*, *44*). This observation may require some dynamic subsidence of relatively shallow material, since the characteristic cooling length scale for the young (<10 My) JdF plate is ≤20 km. Downward advection of (seismically faster) dehydrated mantle would produce a similar signal. Buoyant upwelling also explains a narrow electrical conductivity anomaly at the EPR (*43*) and has been invoked to explain asymmetric melt production (*3*, *18*) suggested, although not demanded, by our data.

If dynamic upwelling takes place at other ridges, then it would offset ocean cooling models by imposing a boundary condition that is different from what is implicitly assumed for conductive half-space cooling. Our data place new constraints on models of MOR topography, which must account for a deep, low-viscosity subaxial region. Effects of dynamic upwelling likely compete with elastic stresses and hydrothermal circulation, which dominate 0- to 2-My ridge morphology (*45*, *46*). It is an open question whether a dynamic subsidence effect is discernible in heat flow data at this or other similar slow-spreading ridges. Our measurements call for renewed investigation of the role of dynamic MOR upwelling and its lasting thermal consequences as plates age. In concert with lateral focusing mechanisms, melt-driven dynamic upwelling explains both narrow melt production at ridges and the deep, narrow region of high attenuation identified for the first time in this study.

MATERIALS AND METHODS

Measuring differential attenuation

We collected *P*- and *S*-wave data from global $M_W > 6.25$ teleseismic (Δ = 25° to 90°) earthquakes recorded on Cascadia Initiative OBS stations (IRIS Network codes 7A, 7D, and X9) between 24 August 2011 and 23 June 2014, windowing by hand to avoid interference from core phases.

Instrument response was removed, and seismograms were integrated to displacement before we corrected for instrument orientation by using best-fitting correction azimuths determined by maximizing receiver function radial components (*47*) or Rayleigh wave polarization [OBSIP (Ocean Bottom Seismograph Instrument Pool) Cascadia Horizontal Orientation Reports 2011–2012, 2012–2013, and 2013–2014]. We measured differential travel times (δT) using cross-correlation (*48*) with a 0.2- to 1-Hz filter (*P* waves) or a 0.083- to 1-Hz filter (*S* waves) applied to a handpicked window around the first arrival, having corrected for move-out using the IASP91 model (*49*). Traces with signal-to-noise ratio smaller than 10 were discarded; the mean cross-correlation coefficient of accepted results was 87% for *S* waves and 86% for *P* waves. Differential t^* was computed pairwise between all combinations of stations by selecting a 35-s window starting 5 s before the predicted body wave arrival and applying a comb of 30 narrow-band filters spaced equally in center frequency from 0.05 to 1 Hz. Several frequency bands between 0.033 and 1 Hz were tested; 0.05 to 1 Hz produced the most consistent measurements between events and smoothly varying profiles of Δt^* with crustal age. At each frequency, the phase shift ($\Delta\psi_{ij}$) and amplitude ratio (R_{ij}) that best transformed trace *i* to match trace *j* were computed to construct the relative phase and amplitude spectra, $\Delta\psi_{ij}(\omega)$ and $R_{ij}(\omega)$, and a vector of weights equal to the final correlation coefficient between *i* and optimally transformed *j*. Frequencies for which the *i*-*j* cross-correlation coefficient was less than 50% were discarded. We also discarded frequencies for which the signal did not exceed the pre-event noise. If fewer than five frequencies in the comb satisfied the criteria, then that station-station pair was ignored. By assuming that effects of attenuation may be expressed in the frequency domain by the delayed attenuation operator and accounting for frequency dependence of the form $Q = Q_0(f/f_0)^{\alpha}$ (*50*), we obtain

$$\ln(R) = k_1 - \pi f_0^{\alpha} f^{1-\alpha} \Delta t_0^* \quad (1)$$

$$\Delta\psi = k_2 + \frac{1}{2}\cot\frac{\alpha\pi}{2} f_0^{\alpha} f^{-\alpha} \Delta t_0^* \quad (2)$$

where *f* are the center frequencies of each filter in the comb and k_1 and k_2 are constants related to the difference in gain between the two stations and differences in anharmonic wave speed, respectively. f_0 is the reference frequency (1 Hz), and Δt_0^* is the value of differential attenuation corrected to that frequency. The subscript "0" was dropped in the main paper. t^* is defined as $l/(V \cdot Q)$, where *l* is path length, and *V* is velocity. We computed Δt^* at each station by a one-step constrained least-squares fitting of all of the pairwise differential amplitude and phase measurements, weighting as above. We did not further interpret the station gain terms. The non–co-temporal northern (years 1 and 3) and southern (year 2) deployments were linked by land stations that recorded throughout. These expressions are nonlinear functions of the frequency exponent, α; we performed a grid search over values of α in the range 0 to 0.9, seeking the value that minimized the global misfit to all station-station differential amplitude and phase measurements (including both land and OBS stations). We found a weak minimum misfit at $\alpha = 0.2$, ruling out $\alpha > 0.6$ at the 1σ level and $\alpha > 0.9$ at the 2σ level. This value is consistent with previous experimental observations (*16*, *17*) and seismological estimates (*15*). For consistency with mineral physics anelastic scaling relationships, we assumed $\alpha = 0.27$ (*16*).

Linear fitting of Δt_S^* versus Δt_P^* and of δT_S versus δT_P was conducted by orthogonal regression. Confidence intervals for the fitted gradients were obtained via bootstrapping.

Calculating attenuation

To calculate Q_S and anelastic shear modulus, we used scaling relationships parameterized using an extended Burgers model, calibrated to the fits of Faul and Jackson (*30*), following Abers *et al.* (*26*). Assuming all viscous and viscoelastic processes scale similarly (*26*, *51*), the effects of melt, water, and grain size were incorporated by scaling relaxation time scales for all processes (τ) involved in the anelasticity calculation

$$\tau = x_{\phi} \left(\frac{C_{OH}}{C_{OH_R}}\right)^{r} d^{m}\, \tau_0(P, T) \quad (3)$$

where $r = 1.0$, $m = 3$, and $\tau_0(P, T)$ is a simple Arrhenius function (*16*). The fits of Faul and Jackson (*30*) have been superseded in the mineral physics literature by Jackson and Faul (*16*), but the later calibrations provided markedly worse agreement to seismological observations, when extrapolated to upper mantle conditions. For completeness, we also computed predicted attenuation and travel time assuming the Jackson and Faul (*16*) fits (see the Supplementary Materials); the diminished attenuation at given (*P*, *T*, *d*) computed using these fits requires larger effect from melt to match the observations and predicts more than three orders of magnitude reduction in diffusion creep shear viscosity.

We computed predicted Δt^* and δT at a range of distances from the ridge axis by propagating rays through a simple two-dimensional MOR model, specifying pressure (*P*), temperature (*T*), grain size (*d*), water (C_{OH}), and melt fraction (ϕ) fields. We computed Q_S and V_S at 3-km increments (*l*) along each ray path. $Q(\omega)$ was used to calculate the amplitude reduction, $A/A_0 = \exp(l\omega/2VQ)$, in each increment as a function of frequency between 0.25 and 0.05 Hz (roughly the same as our observations). Finally, $t^*(\omega)$ for each ray path was calculated by fitting a spectral slope to the amplitude spectrum, assuming $\alpha = 0.27$; this approach was designed to match our measurement technique as closely as possible, to facilitate a more robust comparison between synthetic and observed data. This method approximates the approach of Bellis and Holtzman (*52*). We also report 1-Hz $\delta T_{P,S}$.

Grain size, *d*, was computed using the paleowattmeter (*53*), augmenting grain growth parameters to account for water concentration (*26*, *54*). We computed strain rates assuming that a half-spreading rate of 30 mm/year is accommodated over a 100-km-thick layer, giving $\dot{\epsilon} \approx 10^{-14}\ s^{-1}$. Drawing on the models of Turner *et al.* (*32*), we fixed strain rates in regions of $T < 800$°C to $10^{-19}\ s^{-1}$.

Anharmonic elastic moduli as functions of *P*, *T* were obtained using the HeFESTo package (*55*), assuming a pyrolite composition. Absent data on aggregates or other mineral phases, we assumed that anelasticity for the bulk composition follows that of olivine (*51*).

Two classes of mechanisms for melt-induced attenuation have been proposed: those that rely on intergranular fluid flow ("melt squirt") (*56*) and those in which melt enhances the grain boundary diffusional processes thought to be responsible for high-temperature attenuation (*57*). Forward models indicate that melt squirt, which would produce a distinct high-frequency absorption peak in the absorption spectrum (*56*), cannot yield the observed high attenuation. We found that any large high-frequency absorption peak (*58*, *59*) will cause excessive modulus dispersion, inconsistent with measured travel times and phase spectra. An analytically derived peak attributed to one large pore for 3% melt (*56*) would yield an order of magnitude too little attenuation.

Rather, we simulated the effect of melt in the region by accounting for its influence on diffusivity and hence diffusion creep viscosity (see

the Supplementary Materials) (*57*). We also included the small anharmonic velocity perturbation due to poroelastic effects (*60*). Geochemical and textural data imply that only small in situ melt fractions persist beneath MORs, because high wetting angles permit efficient melt drainage. We introduced a number of different partial melt regions within a 140-km-wide upwelling zone, as follows: Between depths of 180 and 120 km, we assumed 0.01% carbonatite melt (*23*). From depths of 120 to 60 km, we assumed that hydrous melting produces a melt fraction that increases exponentially from 0.01 to 0.2% (*61*). Above this depth, we assumed dry melting, parameterized as a linear increase of melt fraction from 0.2% at 60 km to 2% melt at the surface (*3*). We also included a narrow triangle of ponded melt (ϕ = 1%) at a depth of <45 km beneath the plates (defined by the 1300°C isotherm) (*32*).

SUPPLEMENTARY MATERIALS

Supplementary material for this article is available at http://advances.sciencemag.org/cgi/content/full/3/5/e1602829/DC1

fig. S1. Example of a station-pair differential attenuation measurement using amplitude and phase spectra.
fig. S2. Example of an attenuated *S* wave recorded across the OBS array, with amplitude and phase spectra computed as a function of age.
fig. S3. *S*-wave attenuation measurements for the event shown in fig. S2.
fig. S4. *S*-wave ray paths and attenuation for a southern JdF transect.
fig. S5. Best-fitting attenuation frequency exponent (α).
fig. S6. *S*-wave attenuation for across the array, including results on land.
fig. S7. Differential attenuation and travel time for *P* waves as a function of age.
fig. S8. Trends of Δt_S^* versus Δt_P^* and δT_S versus δT_P.
fig. S9. Example of absolute *S*-wave amplitudes to test long-period focusing.
table S1. Forward models for differential attenuation and travel time at an MOR using anelastic scaling relationships from Jackson and Faul (*16*).
References (*62*–*69*)

REFERENCES AND NOTES

1. J. P. Canales, R. S. Detrick, S. M. Carbotte, G. M. Kent, J. B. Diebold, A. Harding, J. Babcock, M. R. Nedimović, E. van Ark, Upper crustal structure and axial topography at intermediate spreading ridges: Seismic constraints from the southern Juan de Fuca Ridge. *J. Geophys. Res.* **110**, B12104 (2005).
2. S. M. Carbotte, M. R. Nedimovic, J. P. Canales, G. M. Kent, A. J. Harding, M. Marjanović, Variable crustal structure along the Juan de Fuca Ridge: Influence of on-axis hot spots and absolute plate motions. *Geochem. Geophys. Geosyst.* **9**, Q08001 (2008).
3. R. F. Katz, Porosity-driven convection and asymmetry beneath mid-ocean ridges. *Geochem. Geophys. Geosyst.* **11**, Q0AC07 (2010).
4. J. P. Morgan, E. M. Parmentier, J. Lin, Mechanisms for the origin of mid-ocean ridge axial topography: Implications for the thermal and mechanical structure of accreting plate boundaries. *J. Geophys. Res.* **92**, 12823–12836 (1987).
5. D. W. Sparks, E. M. Parmentier, Melt extraction from the mantle beneath spreading centers. *Earth Planet. Sci. Lett.* **105**, 368–377 (1991).
6. B. K. Holtzman, D. L. Kohlstedt, M. E. Zimmerman, F. Heidelbach, T. Hiraga, J. Hustoft, Melt segregation and strain partitioning: Implications for seismic anisotropy and mantle flow. *Science* **301**, 1227–1230 (2003).
7. M. Spiegelman, P. B. Kelemen, E. Aharonov, Causes and consequences of flow organization during melt transport: The reaction infiltration instability in compactible media. *J. Geophys. Res.* **106**, 2061–2077 (2001).
8. D. W. Forsyth, Geophysical constraints on mantle flow and melt generation beneath mid-ocean ridges. *Geophys. Monogr.* **71**, 1–65 (1992).
9. W. C. Hammond, D. R. Toomey, Seismic velocity anisotropy and heterogeneity beneath the Mantle Electromagnetic and Tomography Experiment (MELT) region of the East Pacific Rise from analysis of *P* and *S* body waves. *J. Geophys. Res.* **108**, 2176 (2003).
10. K. Key, S. Constable, L. Liu, A. Pommier, Electrical image of passive mantle upwelling beneath the northern East Pacific Rise. *Nature* **495**, 499–502 (2013).
11. M. Nettles, A. M. Dziewoński, Radially anisotropic shear velocity structure of the upper mantle globally and beneath North America. *J. Geophys. Res.* **113**, B02303 (2008).
12. C. A. Dalton, G. Ekström, A. M. Dziewonski, Global seismological shear velocity and attenuation: A comparison with experimental observations. *Earth Planet. Sci. Lett.* **284**, 65–75 (2009).
13. Y. Yang, D. W. Forsyth, D. S. Weeraratne, Seismic attenuation near the East Pacific Rise and the origin of the low-velocity zone. *Earth Planet. Sci. Lett.* **258**, 260–268 (2007).
14. D. R. Toomey, R. M. Allen, A. H. Barclay, S. W. Bell, P. D. Bromirski, R. L. Carlson, X. Chen, J. A. Collins, R. P. Dziak, B. Evers, D. W. Forsyth, P. Gerstoft, E. E. E. Hooft, D. Livelybrooks, J. A. Lodewyk, D. S. Luther, J. J. McGuire, S. Y. Schwartz, M. Tolstoy, A. M. Tréhu, M. Weirathmueller, W. S. D. Wilcock, The Cascadia Initiative: A sea change in seismological studies of subduction zones. *Oceanography* **27**, 138–150 (2014).
15. V. Lekić, J. Matas, M. Panning, B. Romanowicz, Measurement and implications of frequency dependence of attenuation. *Earth Planet. Sci. Lett.* **282**, 285–293 (2009).
16. I. Jackson, U. H. Faul, Grainsize-sensitive viscoelastic relaxation in olivine: Towards a robust laboratory-based model for seismological application. *Phys. Earth Planet. Inter.* **183**, 151–163 (2010).
17. C. McCarthy, Y. Takei, T. Hiraga, Experimental study of attenuation and dispersion over a broad frequency range: 2. The universal scaling of polycrystalline materials. *J. Geophys. Res.* **116**, B09207 (2011).
18. S. Bell, Y. Ruan, D. W. Forsyth, Ridge asymmetry and deep aqueous alteration at the trench observed from Rayleigh wave tomography of the Juan de Fuca plate. *J. Geophys. Res. Solid Earth* **121**, 7298–7321 (2016).
19. Y. K. Hwang, J. Ritsema, S. Goes, Global variation of body-wave attenuation in the upper mantle from teleseismic P wave and S wave spectra. *Geophys. Res. Lett.* **38**, L06308 (2011).
20. D. L. Anderson, A. Ben-Menahem, C. B. Archambeau, Attenuation of seismic energy in the upper mantle. *J. Geophys. Res.* **70**, 1441–1448 (1965).
21. A. M. Dziewonski, D. L. Anderson, Preliminary reference Earth model. *Phys. Earth Planet. Inter.* **25**, 297–356 (1981).
22. W. C. Hammond, E. D. Humphreys, Upper mantle seismic wave velocity: Effects of realistic partial melt geometries. *J. Geophys. Res.* **105**, 10975–10986 (2000).
23. R. Dasgupta, A. Mallik, K. Tsuno, A. C. Withers, G. Hirth, M. M. Hirschmann, Carbon-dioxide-rich silicate melt in the Earth's upper mantle. *Nature* **493**, 211–215 (2013).
24. M. P. Flanagan, D. A. Wiens, Radial upper mantle attenuation structure of inactive back arc basins from differential shear wave measurements. *J. Geophys. Res.* **99**, 15469–15485 (1994).
25. S. Goes, J. Armitage, N. Harmon, H. Smith, R. Huismans, Low seismic velocities below mid-ocean ridges: Attenuation versus melt retention. *J. Geophys. Res.* **117**, B12403 (2012).
26. G. A. Abers, K. M. Fischer, G. Hirth, D. A. Wiens, T. Plank, B. K. Holtzman, C. McCarthy, E. Gazel, Reconciling mantle attenuation-temperature relationships from seismology, petrology, and laboratory measurements. *Geochem. Geophys. Geosyst.* **15**, 3521–3542 (2014).
27. P. G. Richards, W. Menke, The apparent attenuation of a scattering medium. *Bull. Seismol. Soc. Am.* **73**, 1005–1021 (1983).
28. E. Wielandt, Propagation and structural interpretation of non-plane waves. *Geophys. J. Int.* **113**, 45–53 (1993).
29. R. M. Allen, G. Nolet, W. J. Morgan, K. Vogfjörd, B. H. Bergsson, P. Erlendsson, G. R. Foulger, S. Jakobsdóttir, B. R. Julian, M. Pritchard, S. Ragnarsson, R. Stefánsson, The thin hot plume beneath Iceland. *Geophys. J. Int.* **137**, 51–63 (1999).
30. U. H. Faul, I. Jackson, The seismological signature of temperature and grain size variations in the upper mantle. *Earth Planet. Sci. Lett.* **234**, 119–134 (2005).
31. K. Priestley, D. McKenzie, The relationship between shear wave velocity, temperature, attenuation and viscosity in the shallow part of the mantle. *Earth Planet. Sci. Lett.* **381**, 78–91 (2013).
32. A. J. Turner, R. F. Katz, M. D. Behn, Grain-size dynamics beneath mid-ocean ridges: Implications for permeability and melt extraction. *Geochem. Geophys. Geosyst.* **16**, 925–946 (2015).
33. D. A. Wark, E. B. Watson, Effect of grain size on the distribution and transport of deep-seated fluids and melts. *Geophys. Res. Lett.* **27**, 2029–2032 (2000).
34. U. H. Faul, D. Scott, Grain growth in partially molten olivine aggregates. *Contrib. Mineral. Petrol.* **151**, 101–111 (2005).
35. Y. Aizawa, A. Barnhoorn, U. H. Faul, J. D. F. Gerald, I. Jackson, I. Kovács, Seismic properties of Anita Bay Dunite: An exploratory study of the influence of water. *J. Petrol.* **49**, 841–855 (2008).
36. J. P. Morgan, The generation of a compositional lithosphere by mid-ocean ridge melting and its effect on subsequent off-axis hotspot upwelling and melting. *Earth Planet. Sci. Lett.* **146**, 213–232 (1997).
37. P. D. Asimow, J. E. Dixon, C. H. Langmuir, A hydrous melting and fractionation model for mid-ocean ridge basalts: Application to the Mid-Atlantic Ridge near the Azores. *Geochem. Geophys. Geosyst.* **5**, Q01E16 (2004).
38. C. H. Langmuir, E. M. Klein, T. Plank, *Petrological Systematics of Mid-Ocean Ridge Basalts: Constraints on Melt Generation Beneath Ocean Ridges* (American Geophysical Union, 1993).
39. C. C. Lundstrom, Uranium-series disequilibria in mid-ocean ridge basalts: Observations and models of basalt genesis. *Rev. Mineral. Geochem.* **52**, 175–214 (2003).

40. S. Mei, W. Bai, T. Hiraga, D. L. Kohlstedt, Influence of melt on the creep behavior of olivine–basalt aggregates under hydrous conditions. *Earth Planet. Sci. Lett.* **201**, 491–507 (2002).
41. M. G. Braun, G. Hirth, E. M. Parmentier, The effects of deep damp melting on mantle flow and melt generation beneath mid-ocean ridges. *Earth Planet. Sci. Lett.* **176**, 339–356 (2000).
42. T. Hammouda, S. Keshav, Melting in the mantle in the presence of carbon: Review of experiments and discussion on the origin of carbonatites. *Chem. Geol.* **418**, 171–188 (2015).
43. K. Baba, A. D. Chave, R. L. Evans, G. Hirth, R. L. Mackie, Mantle dynamics beneath the East Pacific Rise at 17°S: Insights from the Mantle Electromagnetic and Tomography (MELT) experiment. *J. Geophys. Res.* **111**, B02101 (2006).
44. N. Harmon, D. W. Forsyth, D. S. Weeraratne, Thickening of young Pacific lithosphere from high-resolution Rayleigh wave tomography: A test of the conductive cooling model. *Earth Planet. Sci. Lett.* **278**, 96–106 (2009).
45. C. J. Grose, J. C. Afonso, Comprehensive plate models for the thermal evolution of oceanic lithosphere. *Geochem. Geophys. Geosyst.* **14**, 3751–3778 (2013).
46. M. A. Eberle, D. W. Forsyth, An alternative, dynamic model of the axial topographic high at fast spreading ridges. *J. Geophys. Res.* **103**, 12309–12320 (1998).
47. H. A. Janiszewski, G. A. Abers, Imaging the plate interface in the Cascadia Seismogenic Zone: New constraints from offshore receiver functions. *Seismol. Res. Lett.* **86**, 1261–1269 (2015).
48. J. C. VanDecar, R. S. Crosson, Determination of teleseismic relative phase arrival times using multi-channel cross-correlation and least squares. *Bull. Seismol. Soc. Am.* **80**, 150–169 (1990).
49. B. L. N. Kennet, E. R. Engdahl, Traveltimes for global earthquake location and phase identification. *Geophys. J. Int.* **105**, 429–465 (1991).
50. J. B. Minster, D. L. Anderson, A model of dislocation-controlled rheology for the mantle. *Philos. Trans. R. Soc. A* **299**, 319–356 (1981).
51. T. M. Olugboji, S. Karato, J. Park, Structures of the oceanic lithosphere-asthenosphere boundary: Mineral-physics modeling and seismological signatures. *Geochem. Geophys. Geosyst.* **14**, 880–901 (2013).
52. C. Bellis, B. Holtzman, Sensitivity of seismic measurements to frequency-dependent attenuation and upper mantle structure: An initial approach. *J. Geophys. Res. Solid Earth* **119**, 5497–5517 (2014).
53. N. J. Austin, B. Evans, Paleowattmeters: A scaling relation for dynamically recrystallized grain size. *Geology* **35**, 343–346 (2007).
54. M. D. Behn, G. Hirth, J. R. Elsenbeck II, Implications of grain size evolution on the seismic structure of the oceanic upper mantle. *Earth Planet. Sci. Lett.* **282**, 178–189 (2009).
55. L. Stixrude, C. Lithgow-Bertelloni, Thermodynamics of mantle minerals—II. Phase equilibria. *Geophys. J. Int.* **184**, 1180–1213 (2011).
56. W. C. Hammond, E. D. Humphreys, Upper mantle seismic wave attenuation: Effects of realistic partial melt distribution. *J. Geophys. Res.* **105**, 10987–10999 (2000).
57. B. K. Holtzman, Questions on the existence, persistence, and mechanical effects of a very small melt fraction in the asthenosphere. *Geochem. Geophys. Geosyst.* **17**, 470–484 (2016).
58. M. Sundberg, R. F. Cooper, A composite viscoelastic model for incorporating grain boundary sliding and transient diffusion creep; correlating creep and attenuation responses for materials with a fine grain size. *Philos. Mag.* **90**, 2817–2840 (2010).
59. Y. Takei, F. Karasawa, H. Yamauchi, Temperature, grain size, and chemical controls on polycrystal anelasticity over a broad frequency range extending into the seismic range. *J. Geophys. Res.* **119**, 5414–5443 (2014).
60. Y. Takei, Effect of pore geometry on V_p/V_s: From equilibrium geometry to crack. *J. Geophys. Res.* **107**, ECV 6-1–ECV 6-12 (2002).
61. G. Hirth, D. L. Kohlstedt, Water in the oceanic upper mantle: Implications for rheology, melt extraction and the evolution of the lithosphere. *Earth Planet. Sci. Lett.* **144**, 93–108 (1996).
62. R. F. Cooper, Seismic wave attenuation: Energy dissipation in viscoelastic crystalline solids. *Rev. Mineral. Geochem.* **51**, 253–290 (2002).
63. Y. Xu, M. E. Zimmerman, D. L. Kohlstedt, Deformation behavior of partially molten mantle rocks, in *Rheology and Deformation of the Lithosphere at Continental Margins*, G. D. Karmer, B. Taylor, N. W. Driscoll, D. L. Kohlstedt, Eds. (Columbia Univ. Press, 2004), pp. 284–410.
64. G. Hirth, D. L. Kohlstedt, Rheology of the upper mantle and the mantle wedge: A view from the experimentalists, in *Inside the Subduction Factory, Geophysical Monograph 138*, J. Eiler, M. Hirschmann, Eds. (American Geophysical Union, 2003).
65. G. Hirth, D. L. Kohlstedt, Experimental constraints on the dynamics of the partially molten upper mantle: Deformation in the diffusion creep regime. *J. Geophys. Res.* **100**, 1981–2001 (1995).
66. C. McCarthy, Y. Takei, Anelasticity and viscosity of partially molten rock analogue: Toward seismic detection of small quantities of melt. *Geophys. Res. Lett.* **38**, L18306 (2011).
67. Y. Takei, B. K. Holtzman, Viscous constitutive relations of solid-liquid composites in terms of grain boundary contiguity: 1. Grain boundary diffusion control model. *J. Geophys. Res.* **114**, B06205 (2009).
68. D. J. Thomson, Spectrum estimation and harmonic analysis. *Proc. IEEE* **70**, 1055–1096 (1982).
69. D. S. Wilson, Confidence intervals for motion and deformation of the Juan de Fuca plate. *J. Geophys. Res.* **98**, 16053–16071 (1993).

Acknowledgments: We acknowledge helpful discussions with B. Holtzman, D. Forsyth, M. Parmentier, J. Gaherty, and S. Wei. Two anonymous reviewers provided insightful and thorough comments. **Funding:** This work was funded by NSF grant OCE #1536566. This is Lamont-Doherty Earth Observatory (LDEO) contribution 8102. **Author contributions:** Z.C.E., mentored by G.A.A., carried out methods development, data analysis, interpretation, figure drafting, and manuscript preparation. G.A.A. also contributed to manuscript editing. **Competing interests:** G.A.A. is Vice Chair, Board of Directors, for Incorporated Research Institutions for Seismology. Z.C.E. declares that he has no competing interests. **Data and materials availability:** All data needed to evaluate the conclusions in the paper are present in the paper and/or the Supplementary Materials. Additional data related to this paper may be requested from the authors. The authors are happy to provide MATLAB scripts used to compute differential attenuation and travel time. All data used are openly available through the IRIS Data Management Center.

Submitted 14 November 2016
Accepted 23 March 2017
Published 24 May 2017
10.1126/sciadv.1602829

Citation: Z. C. Eilon, G. A. Abers, High seismic attenuation at a mid-ocean ridge reveals the distribution of deep melt. *Sci. Adv.* **3**, e1602829 (2017).

High seismic attenuation at a mid-ocean ridge reveals the distribution of deep melt
Zachary C. Eilon and Geoffrey A. Abers (May 24, 2017)
Sci Adv 2017, 3:.
doi: 10.1126/sciadv.1602829